Sampling strategy for the sparse recovery of infrared images

Serdar Cakir,* Hande Uzeler, and Tayfun Aytaç
TÜBİTAK BİLGEM İLTAREN, İlhan Tan Kışlası, Ümitköy, Ankara, Turkey
*Corresponding author: serdar.cakir@tubitak.gov.tr

Received 24 April 2013; revised 6 August 2013; accepted 15 August 2013;
posted 15 August 2013 (Doc. ID 189388); published 24 September 2013

The compressive sensing (CS) framework states that a signal that has a sparse representation in a known basis may be reconstructed from samples obtained at a sub-Nyquist sampling rate. The Fourier domain is widely used in CS applications due to its inherent properties. Sparse signal recovery applications using a small number of Fourier transform coefficients have made solutions to large-scale data recovery problems, including image recovery problems, more practical. The sparse reconstruction of 2D images is performed using the sampling patterns generated by taking the general frequency characteristics of the images into account. In this work, instead of forming a general sampling pattern for infrared (IR) images, a special sampling pattern is obtained by gathering a database to extract the frequency characteristics of IR sea-surveillance images. Experimental results show that the proposed sampling pattern provides better sparse recovery results compared to the widely used patterns proposed in the literature. It is also shown that, together with a certain image dataset, the sampling pattern generated by the proposed scheme can be generalized for various image sparse recovery applications.

OCIS codes: (070.0070) Fourier optics and signal processing; (100.2000) Digital image processing; (100.3190) Inverse problems; (110.1758) Computational imaging; (110.3080) Infrared imaging; (100.3010) Image reconstruction techniques.
http://dx.doi.org/10.1364/AO.52.006858

1. Introduction

According to the Nyquist–Shannon sampling theorem, signal reconstruction is possible when the signal is sampled at twice its maximum frequency. Sampling at this rate provides a large number of samples, which in many applications often necessitates the signal to be compressed before further processing. Increasing sampling rate is often very expensive in imaging systems, such as medical scanners and radars [1]. Recently, it has been shown through the theory of compressive sensing (CS) that signal reconstruction can still be possible when sampling below the Nyquist rate [2,3]. The CS theory enables a sparse or compressible signal to be reconstructed by obtaining a small number of linear projections from that signal. Reconstruction is achieved by carrying out an optimization procedure to recover the original signal from the projections. Due to these attributes, the CS framework is used in many applications, such as imaging systems [4–6], data compression [7,8], image fusion [9,10], remote sensing [11–13], object silhouette extraction [14], motion estimation [15], target tracking [16,17], and automatic target recognition [18].

The CS theory is also used together with the learning concept in the treatment of determining the sensing matrix and/or sparse representation matrix to obtain higher sparse reconstruction performance [19]. In order to obtain such a framework, an image database is used to learn the sensing matrix and sparsifying matrix simultaneously [19]. Although the authors state that they achieve higher reconstruction results, they also point out the computational limitations of their proposed framework [19,20].

1559-128X/13/286858-10$15.00/0

In this work, we propose a new sampling strategy for the sparse recovery of infrared (IR) sea-surveillance images. Instead of sampling the Fourier coefficients of an image using well-known frequency characteristics, the sparse reconstruction of images is carried out by a method that determines the significant frequency characteristics of the image set gathered for maritime surveillance. These frequency characteristics enable cleverly pooling the frequency components present in the images. Here the proposed method for the IR image sparse reconstruction is compared to baseline sampling pattern techniques widely used in CS and experimental results are reported. The proposed method, while shown here for a specific surveillance problem, can also be applied without loss of generality to other image recovery problems when appropriate image datasets are available for the problem of interest.

The paper is organized as follows: Section 2 provides a brief overview of the CS theory. Section 3 surveys the sampling patterns used with the CS framework in the literature. Section 4 presents the details of the proposed sun-shaped pattern, and in Section 5 the experimental methodology, recovery results, and comparative analysis are provided.

2. Compressive Sensing

The CS framework offers a method to directly sense the data in a compressed form, rather than sampling the signal at a high rate and then compressing the sampled data. It has been shown that a finite-dimensional signal having a sparse or compressible representation can be recovered from a small set of linear nonadaptive measurements [2,3]. Recently, researchers have focused on the use of adaptive approaches to determine the measurement matrix [21,22]. In [21], the sparse Bayesian learning theory is incorporated into the CS framework, but it is criticized in several aspects, such as expensive sampling process and arbitrariness in the choice of the priors [23,24].

Let $x \in \mathbb{R}^N$ be a real-valued, finite-length signal. In the case where the signal is an image, the image may be vectorized into a 1D vector. x can be represented in terms of $\{\psi_i\}_{i=1}^N$ basis vectors of dimension $N \times 1$. Arranging the basis vectors as columns of the basis matrix $\Psi = [\psi_1|\psi_2|\ldots|\psi_N]$, x may be represented as shown in Eq. (1):

$$x = \Psi s. \tag{1}$$

The signal x is K sparse if there exist only K nonzero values in the $N \times 1$ vector s, as the signal x may be represented as the linear combination of K basis vectors.

CS systems typically acquire $M < N$ measurements from the signal x in the form of inner products between the signal and a set of sensing vectors [1]. The measurements are equal to the inner product of x with $\{\phi_j\}_{j=1}^M$ measurement vectors such that $y(j) = \langle x, \phi_j^T \rangle$, $j \in \{1, 2, \ldots, M\}$. Arranging the measurement vectors as rows of the matrix Φ, the resultant measurement data y of dimension $M \times 1$ may be expressed as in Eq. (2)

$$y = \Phi x = \Phi\Psi s. \tag{2}$$

The goal is to recover x, or alternatively the sparse coefficients of s from y. Because $M < N$, recovery of the image x from the compressed samples y is ill posed; however, the sparsity assumption and the incoherence of the bases Φ and Ψ make recovery of s possible [25]. These bases are incoherent when the rows of the sparsity basis Φ cannot sparsely represent the columns of the measurement matrix Ψ [26].

The sparse reconstruction of s is achieved by using optimization methods to find the signal $\hat{s}$ that satisfies the measurement data y while minimizing the ℓ_0 norm. However, solving for the ℓ_0 norm is generally an $n - p$ hard problem [8]. One of the most important contributions made by the CS theory is that it is possible to recover the signal using ℓ_1-norm minimization. Therefore the signal may be recovered by solving the following optimization problem:

$$\hat{s} = \arg \min \|s'\|_1 \quad \text{such that } y = \Phi\Psi s'. \tag{3}$$

In our image recovery case, the optimization problem can be rewritten based on the sparsity of the discrete image gradient [27]. The discrete image gradient can be defined as in Eq. (4)

$$\begin{aligned} D_h(i,j) &= \begin{cases} \hat{x}(i,j+1) - \hat{x}(i,j) & i < W \\ 0 & i = W \end{cases} \\ D_v(i,j) &= \begin{cases} \hat{x}(i+1,j) - \hat{x}(i,j) & j < W \\ 0 & j = W \end{cases} \\ \|\hat{x}\|_{\mathrm{TV}} &= \sum_{i=1}^{W}\sum_{j=1}^{W} \sqrt{D_h(i,j)^2 + D_h(i,j)^2}\,. \end{aligned} \tag{4}$$

Here, $\hat{x} \in \mathbb{R}^{W \times W}$ is the 2D recovery matrix, $D_h(i,j)$ and $D_v(i,j)$ horizontal and vertical gradients calculated at location (i,j), and the total-variation norm $\|\hat{x}\|_{\mathrm{TV}}$ is the total sum of discrete image gradients over all the pixel locations. In order to reconstruct the 2D Fourier transform of the image $[X(u,v)]$ from partial Fourier samples $\tilde{X}(u,v)$, the optimization problem provided in Eq. (5) needs to be solved

$$\min \|\hat{x}\|_{\mathrm{TV}} \quad \text{subject to } \hat{X}(u,v) = X(u,v). \tag{5}$$

The optimization problem stated in Eq. (5) is known as Basis Pursuit and may be solved using linear programming techniques. There are many solvers available for recovering the signal from the measurement results using convex programming [28–30]. In this work, the ℓ_1-magic package [30] is selected because it is stated as one of the fastest implementations of the interior-point linear

programming technique [31], and it takes advantage of the ℓ_1-based structure that provides efficient solutions to the corresponding optimization problem.

3. Sampling Patterns in Fourier Basis

Fourier basis vectors together with a certain sampling pattern are often used for the construction of the measurement matrix Φ in sparse recovery applications [2]. The sampling pattern used in such reconstruction schemes directly affects the performance of the reconstruction algorithm. Candes *et al.* suggest a uniform Fourier sampling pattern for CS reconstruction [2]. The image reconstruction results presented in [32] show that the Gaussian random sampling strategy [Fig. 1(b)] outperforms the uniform random sampling technique [Fig. 1(a)] in terms of reconstruction performance. Both sampling strategies are used in three different CS optimization frameworks in order to constitute a detailed performance analysis.

In [2], a structured sampling pattern consisting of 22 radial lines [Fig. 1(c)] is used to demonstrate the reconstruction performance of the CS algorithm. This sampling pattern known as the star-shaped sampling pattern (P_{Star}) samples the low frequencies more densely compared to the high frequencies. In [33], a variable density sampling strategy is proposed by exploiting the statistical distributions of natural images in the wavelet domain as prior information. Pseudorandom undersampling is implemented in [34] by using two independent and uniformly distributed random numbers corresponding to k-space radius and azimuthal angle. Moreover, the low frequencies, whose outermost k-space radius is 30% of the full k-space radius, are fully sampled. This way, the resulting sampling pattern collects more samples at low frequencies.

In [9], two nonuniform sampling patterns, namely the double-star-shaped pattern ($P_{\text{DoubleStar}}$) and the star-circle-shaped pattern ($P_{\text{StarCircle}}$) given in Figs. 1(d) and 1(e), respectively, are proposed. The sparse reconstruction performances of these patterns and the P_{Star} are compared over several images. The authors state that their proposed sampling patterns provide promising results when used in the CS framework for the image fusion problem. Because these patterns provide promising results, they are used as baseline sampling patterns together with the random sampling (P_{Random}) and the Gaussian random sampling (P_{Gauss}) patterns in order to make performance comparisons with our proposed sampling technique described in the next section.

4. Sun-Shaped Nonuniform Sampling Pattern

In this work, instead of using a sampling pattern designed according to the general characteristics of natural images, a specific sampling pattern has been generated by using the frequency information extracted from an image database consisting of images captured by an IR imaging system. The sampling pattern generation using the image database can be thought of as the learning phase in machine vision theory. By introducing such a training phase, a system-specific solution is achieved that leads to better sparse recovery performance.

The proposed sampling pattern extraction scheme tries to determine the important frequency components by interpreting the frequency characteristics of the IR images in the database. In this context, the 2D Fourier transform of each image $X_t(u,v)$ is calculated as in Eq. (6) in order to obtain a general frequency characteristic:

$$X_t(u,v) = \frac{1}{WH}\sum_{m=0}^{H-1}\sum_{n=0}^{W-1} x_t(m,n)e^{-j2\pi\left(\frac{um}{H}+\frac{vn}{W}\right)}. \quad (6)$$

Here, $x_t(m,n)$ $(t = 1,2,\ldots,\beta)$ is an $H \times W$ dimensional image from the database. $x_t(m,n)$ denotes the pixel value located at the mth row and the nth column of the image. β stands for the number of images in the dataset.

The general frequency characteristics of the IR images $[\tilde{X}_{\text{ave}}(u,v)]$ in the database are obtained by averaging the magnitudes of each $X_t(u,v)$ as given in Eq. (7):

$$\tilde{X}_{\text{ave}}(u,v) = \frac{1}{\beta}\sum_{t=1}^{\beta} |X_t(u,v)|. \quad (7)$$

$\tilde{X}_{\text{ave}}(u,v)$ is used in an iterative framework designed to generate the sampling pattern. The main steps of this iterative technique are presented in Fig. 2.

The iterative algorithm is based on sampling the Fourier domain with a different rate at each iteration. In the first iteration, $\tilde{X}_{\text{ave}}(u,v)$ is not exposed to masking, but in further iterations $\tilde{X}_{\text{ave}}(u,v)$ is

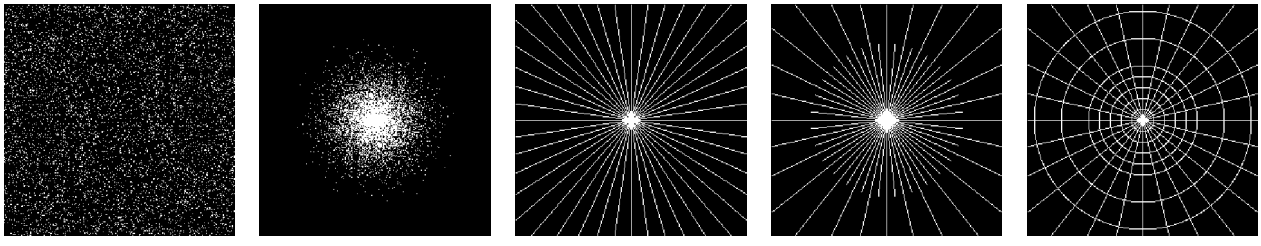

(a) P_{Random} (b) P_{Gauss} (c) P_{Star} (d) $P_{DoubleStar}$ (e) $P_{StarCircle}$

Fig. 1. Uniform and nonuniform sampling patterns.

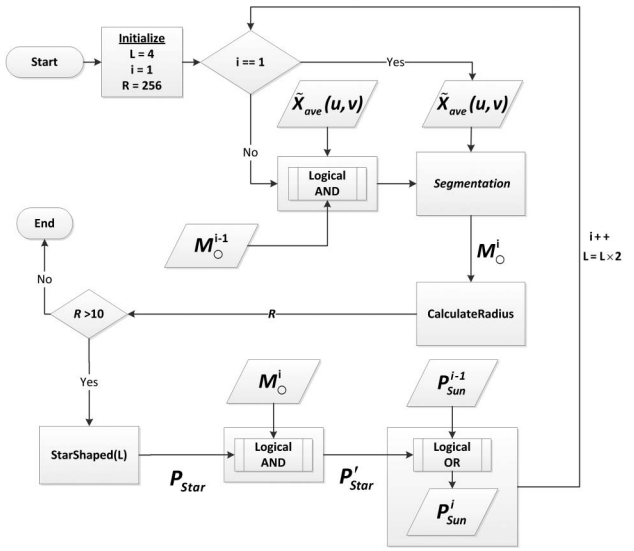

Fig. 2. Flow diagram of the sun-shaped sampling pattern generation technique.

masked with the circular mask generated in the previous iteration. The segmentation process is performed on the "Segmentation" block given in Fig. 2. In this block, the mean (μ) and standard deviation (σ) values of the masked $\tilde{X}_{\text{ave}}(u,v)$ are computed. These values are used to calculate the threshold (τ_{seg}) used in the segmentation:

$$\tau_{\text{seg}} = \mu + \kappa\sigma. \tag{8}$$

Here, μ and σ are the first- and second-order statistics of $\tilde{X}_{\text{ave}}(u,v)$ and κ is the coefficient to adjust the threshold to a desired level.

After the calculation of τ_{seg}, the masked $\tilde{X}_{\text{ave}}(u,v)$ is segmented. The segmentation result is used to generate a circular mask with radius R at the ith iteration ($M^i_{\bigcirc}$) that is used to discard the insignificant frequency components. The radius R of $M^i_{\bigcirc}$ is calculated at the "CalculateRadius" block as the length of the minor axis of the segmented blob. After the computation of $M^i_{\bigcirc}$, the next step is to update the P^i_{Sun} using the masked version of the star-shaped pattern (P_{star}). The P_{star} generation is performed at the "StarShaped(L)" block presented in Fig. 2. In this block, the classical P_{star} is formed over L radial lines. Then, the undesired frequency components are eliminated by applying $M^i_{\bigcirc}$ to P_{star}. The masked P'_{star} at each iteration is exposed to a logical OR operation with matrix P^{i-1}_{Sun} that is used to form the P_{Sun}.

Initially, each element of the matrix P^i_{Sun} is set to zero. At each iteration, P^i_{Sun} is updated with the masked P'_{star}. After P^i_{Sun} is updated, the algorithm proceeds to the next iteration by incrementing the iteration index i and doubling the P_{star} generation rate (L). This way, the algorithm samples the lower frequencies more densely. This is achieved with the increase in L and the decrease in R. As an example, the P_{star} computed at each of the six iterations is illustrated in Fig. 3.

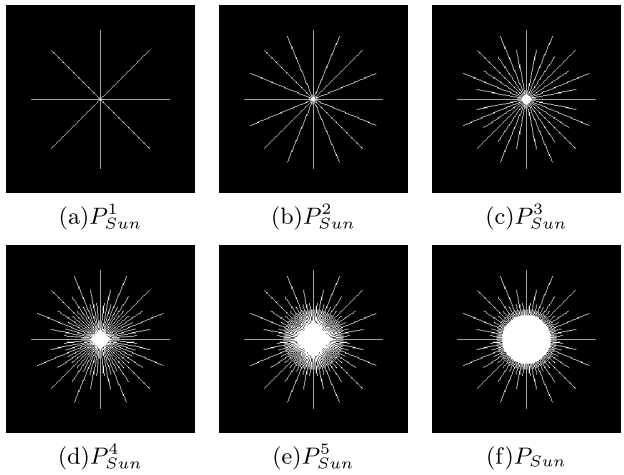

Fig. 3. Illustration of the sun-shaped pattern at each iteration (P^i_{Sun}) of the algorithm for $i = 1, 2, 3, 4, 5, 6$.

At the end of the iterative algorithm, the P_{Sun} is obtained as presented in Fig. 3(f). P_{Sun} takes more samples at low frequencies compared to higher frequencies. However, the proposed pattern selectively takes into account the higher frequency components where edges may lie and sharp changes may occur.

For the sake of completeness of the algorithm discussion, the algorithm block for the computation of the P_{sun} is summarized in the algorithm block given in Algorithm 1.

Algorithm 1 P_{Sun} generation algorithm

input: $\tilde{X}_{\text{ave}}(u,v)$
output: P_{Sun}
initialization
$L \leftarrow 4$;
$i \leftarrow 1$;
$R \leftarrow 256$;
while $R > 10$ **do**
  if $i = 1$ **then**
    $M^i_{\bigcirc} \leftarrow \text{Segmentation}(\tilde{X}_{\text{ave}}(u,v))$;
  else
    $M^i_{\bigcirc} \leftarrow \text{Segmentation}(M^{i-1}_{\bigcirc} \wedge \tilde{X}_{\text{ave}}(u,v))$;
  end if
  $R \leftarrow \text{CalculateRadius}(M^i_{\bigcirc})$;
  if $R > 10$ **then**
    $P_{\text{Star}} \leftarrow \text{StarShaped}(L)$;
    $P'_{\text{Star}} \leftarrow P_{\text{Star}} \wedge M^i_{\bigcirc}$;
    if $i = 1$ **then**
      $P^i_{\text{Sun}} \leftarrow P'_{\text{Star}}$;
    else
      $P^i_{\text{Sun}} \leftarrow P'_{\text{Star}} \vee P^{i-1}_{\text{Sun}}$;
    end if
    $i \leftarrow i + 1$;
    $L \leftarrow L \times 2$;
  end if
end while
$P_{\text{Sun}} \leftarrow P^i_{\text{Sun}}$;
return P_{Sun};

5. Performance Comparisons

First, the image dataset used for the extraction of the frequency characteristics is briefly mentioned. Then,

the experiments carried out to compare the performance of the proposed method with those of the baseline techniques are explained in detail.

A. Image Database

In the experiments, the frequency characteristics of sea-surveillance images captured in the IR band are extracted by using the methodology explained in Section 4. In this context, eight different sea-surveillance scenarios consisting of 483 images of resolution 140 × 276 captured by a camera operating in the 8–12 μm IR band are used. Several sample IR images present in the dataset are shown in Fig. 4. In addition to the sea-surface platforms, other objects, such as seagulls, an electric rod, land background, and so forth are also present in the images. These factors cause partial occlusion in certain frames, which is a major difficulty in determining the frequency characteristics of IR sea-surface target images.

The images in the database are initially resized to 130 × 256 while preserving the aspect ratio and are normalized to the [0–1] interval. The images are then padded with zero blocks to make the image size 256 × 256, because the fast Fourier transform is computed efficiently if the dimensions of the input image can be expressed as a power of 2. The resizing and zero-padding operations are performed in order to establish a fair comparison between the proposed method and the baseline techniques because these previously published baseline techniques [2,9] use 256 × 256 images in the sparse reconstruction problem.

B. Experiments

By using the algorithm presented in Section 4 and the database detailed in Section 5.A, the P_{Sun} pattern illustrated in Fig. 3(f) is obtained. The threshold constant κ is selected as 0.103 after a large-scale cross-validation process. In the cross-validation phase, the sparse recovery of a group of input images is repeated for a large and dense set of κ values. The κ value providing the best recovery performance is fixed for the whole experimental studies.

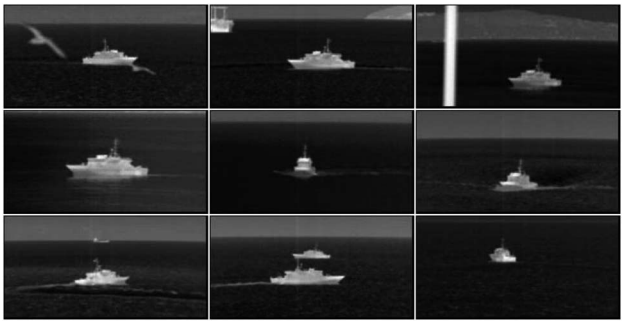

Fig. 4. Sample IR images from the image dataset.

As an additional constraint, the number of samples obtained by the specific choice of κ should not exceed the number of samples present in the P_{Star} pattern calculated over 22 radial lines.

The "tveq_logbarrier" optimization subroutine in the ℓ_1-magic package, enabling the barrier iterations for equality constrained total variation minimization, is preferred in the experiments carried out within the scope of this work. The log-barrier method, which follows the generic (but effective) algorithm described in [35], is conceptually more straightforward than the primal-dual method [35], but at its core, it solves for a series of Newton steps. The "tveq_logbarrier" subroutine requires four parameters; namely, desired precision, iteration growth, Newton step precision, and iteration limit. In the experiments, these parameters are selected as 0.1, 2, 10^{-8}, and 600, respectively.

In the experiments, the image reconstruction performance of the proposed pattern is compared with the performances of the P_{Random}, P_{Gauss}, P_{Star} calculated over 22 radial lines, $P_{\text{DoubleStar}}$, and $P_{\text{StarCircle}}$ sampling patterns. The number of samples present in these sampling patterns is listed in Table 1.

In the performance comparisons, peak signal-to-noise ratio (PSNR) is used as a performance measure. Another performance measure used in the experiments is the "universal image quality index" (UIQI) [36]. This quality index, which takes values in the [−1, 1] interval, is computed as shown in Eq. (9):

$$Q = \left(\frac{\sigma_{xx_{\text{recons}}}}{\sigma_x \sigma_{x_{\text{recons}}}}\right)\left(\frac{2\bar{x}\bar{x}_{\text{recons}}}{\bar{x}^2 + (\bar{x}_{\text{recons}})^2}\right)\left(\frac{2\sigma_x \sigma_{x_{\text{recons}}}}{\sigma_x^2 + \sigma_{x_{\text{recons}}}^2}\right). \quad (9)$$

Here, $\sigma_{xx_{\text{recons}}}$ is the cross correlation between the original image and the recovered image, and σ_x and $\sigma_{x_{\text{recons}}}$ are the standard deviations of the original and the recovered images, respectively. The mean values of the original and the recovered images are denoted by $\bar{x}$ and $\bar{x}_{\text{recons}}$. The quality index measures the quality of the reconstructed image by

Table 1. Sample Sizes of Each Sampling Pattern and the Corresponding Average PSNR and UIQI Values for Experiments 1 and 2

Sampling Pattern	Number of Samples	Average PSNR (dB)		UIQI	
		Exp. 1	Exp. 2	Exp. 1	Exp. 2
P_{Random}	2883	27.055	22.610	0.231	0.166
P_{Star}	2740	37.578	38.117	0.588	0.678
$P_{\text{DoubleStar}}$	2744	38.583	38.949	0.657	0.719
$P_{\text{StarCircle}}$	2896	37.211	37.801	0.562	0.658
P_{Gauss}	2283	38.613	39.946	0.776	0.785
Proposed P_{Sun}	2226	39.512	39.948	0.829	0.840

evaluating the "loss of correlation," "luminance distortion," and "contrast distortion" terms [36]. Subsequently, these terms are multiplicatively combined in order to achieve a quality score defined as the universal quality index. Note that the quality index becomes one if the input image and reconstructed image are identical. Therefore, higher values of quality index are a simple indicator of better sparse image recovery.

1. *Experiment 1*

In the first experiment, the sparse reconstruction of 82 IR sea-surveillance platform images captured using the same IR camera mentioned in Section 5.A is performed. These images were captured within three different sea-surface surveillance scenarios. The sparse recovery is carried out using the proposed sampling pattern and the baseline sampling patterns. The reconstruction performances of the proposed and baseline sampling patterns are evaluated by computing the PSNR and the UIQI of each reconstructed image.

The PSNRs of the images constructed using different sampling patterns are shown in Fig. 5. The average PSNRs and average UIQI values corresponding to each sampling pattern are provided in Table 1, and examples of reconstruction results for each sampling pattern are visualized in Fig. 6. Moreover, the zoomed reconstruction results of a test image are also shown in Fig. 7 in order to observe how the structural details within the image are preserved.

By looking at the reconstruction results presented in Figs. 5 and 7, and Table 1, one can say that the proposed sampling scheme outperforms the baseline sampling strategies. Furthermore, the proposed P_{sun} includes fewer samples than the baseline sampling methods. From Fig. 6, it can be observed that the reconstructed images formed by using the proposed sampling strategy preserve the detailed texture information that lies in the high frequencies of the original image. The image details are preserved by combining the high-frequency coefficients with the low-frequency terms in an efficient manner. Therefore, the technique proposed herein enables better sparse recovery performance with fewer samples compared to the baseline methods.

In order to investigate and visualize the frequency domain coverage of the sampling patterns further, an error image $|\text{FFT}\{x - x_{\text{recons}}\}|$ is provided in Fig. 8 for each radial sampling regime.

By looking at the error images presented in Fig. 8, one can say that the error values for P_{Sun} are mainly zero, especially at low frequencies, because P_{Sun} covers more low-frequency components than other sampling regimes. The P_{Sun} sampling framework also collects samples at high frequencies in a clever manner. This way, the edges and structural information are better preserved, which leads to higher recovery performance. Also note that the error image computed for the random sampling strategy is not visualized in Fig. 8 because the random sampling technique does not provide comparable reconstruction performance with the radial sampling schemes.

2. *Experiment 2*

In the second experiment, 120 images of resolution 244×324 captured with a camera working in the 8–12 μm IR band are used. Note that the camera and the surveillance scenarios are considerably different from the ones used in the first experiment.

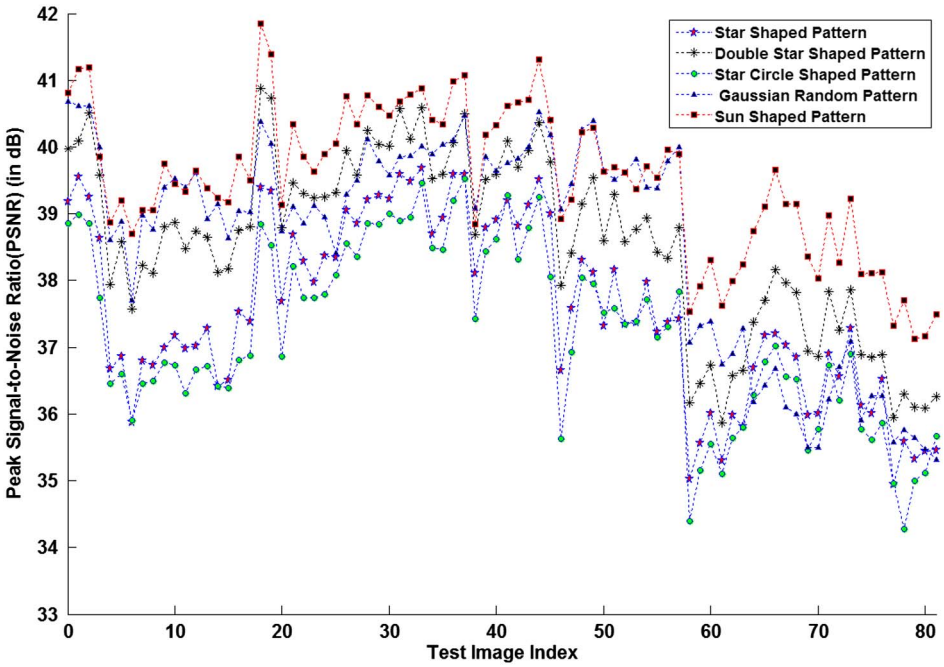

Fig. 5. PSNR ratios of the reconstructed images using different sampling patterns for experiment 1.

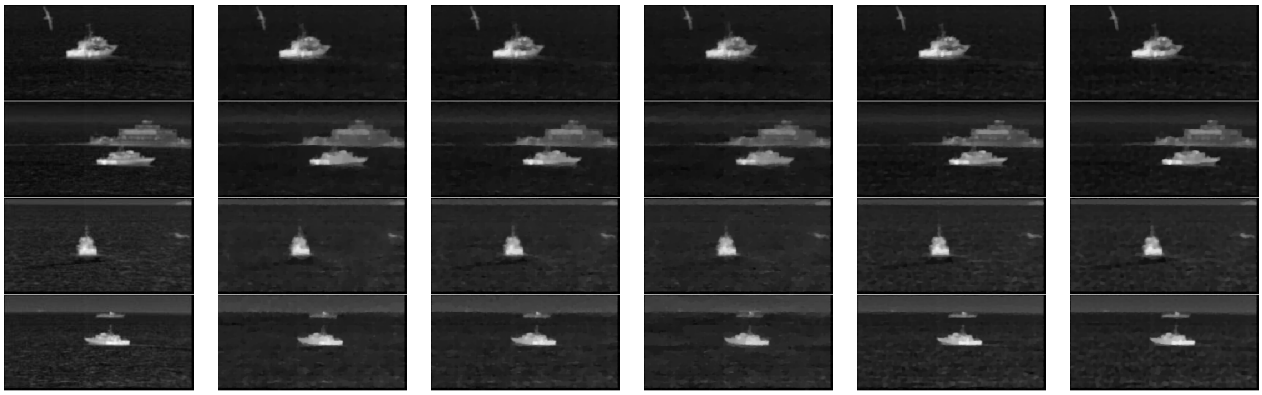

(a)Original (b)P_{Star} (c)$P_{DoubleStar}$ (d)$P_{StarCircle}$ (e)P_{Gauss} (f)P_{Sun}

Fig. 6. Examples of reconstructed images using different sampling patterns for experiment 1.

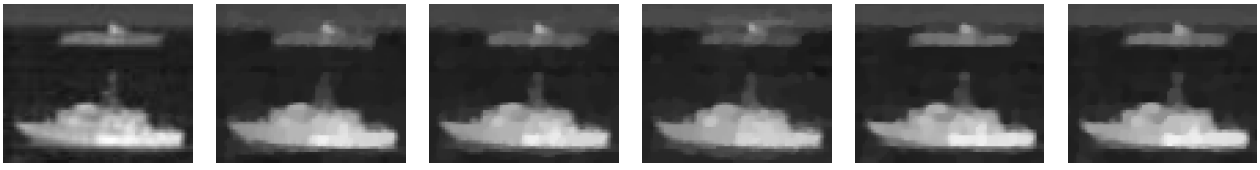

(a)Original (b)P_{Star} (c)$P_{DoubleStar}$ (d)$P_{StarCircle}$ (e)P_{Gauss} (f)P_{Sun}

Fig. 7. Examples of zoomed reconstruction results obtained using different sampling patterns for experiment 1.

In addition, the sea-surface platforms are located at various ranges. The images in this dataset are exposed to the same preprocessing phase performed in the first experiment before being used in the sparse reconstruction problem. As a result, the images obtained are of size 256 × 256. After preprocessing, the test images are reconstructed using the proposed sampling strategy and baseline sampling methods. The reconstructed images formed using different sampling patterns are illustrated in Fig. 9. The corresponding PSNRs and average PSNR values are provided in Fig. 10 and Table 1, respectively. Average UIQI values are also given in Table 1.

By looking at these results one can conclude that the proposed sampling pattern represents the general characteristics of sea-surface targets captured in the 8–12 μm IR band better than the baseline sampling schemes. The proposed pattern not only provides higher reconstruction performance but also reduces the number of samples. Because the proposed P_{sun} pattern collects the high-frequency components in a clever manner, the sharp edges and important texture details still exist in the reconstructed images. Therefore, the distant platforms appearing on/near the horizon are still visible in the images reconstructed using the P_{Sun} pattern, whereas most of the signature coming from the distant platforms decays in the images constructed using the baseline sampling patterns.

In experiments 1 and 2, for the random sampling pattern, the PSNR values of each reconstructed image frame, reconstruction results, and the error analysis image are not provided because the results of the random sampling strategy are significantly worse than those obtained with the other sampling patterns considered in this paper. This is also the case when the autocorrelations of the sampling patterns are analyzed. Because the autocorrelation of the random sampling pattern consists of a single peak centered at the DC location, it can be thought that the reconstruction may suffer from lack of representative frequency components. However, the

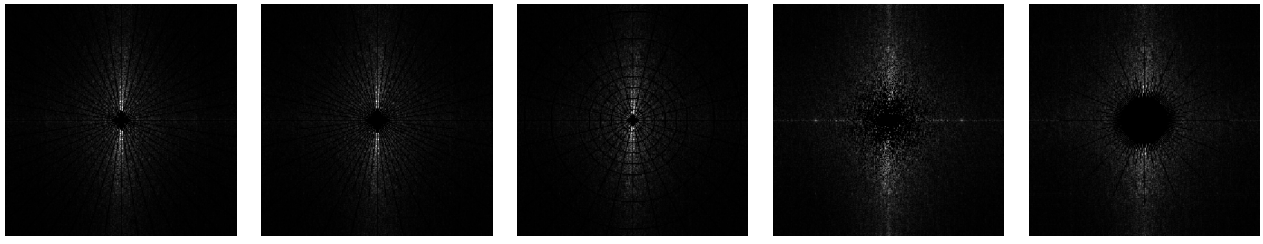

(a)P_{Star} (b)$P_{DoubleStar}$ (c)$P_{StarCircle}$ (d)P_{Gauss} (e)Proposed P_{Sun}

Fig. 8. Error images calculated for radial sampling patterns.

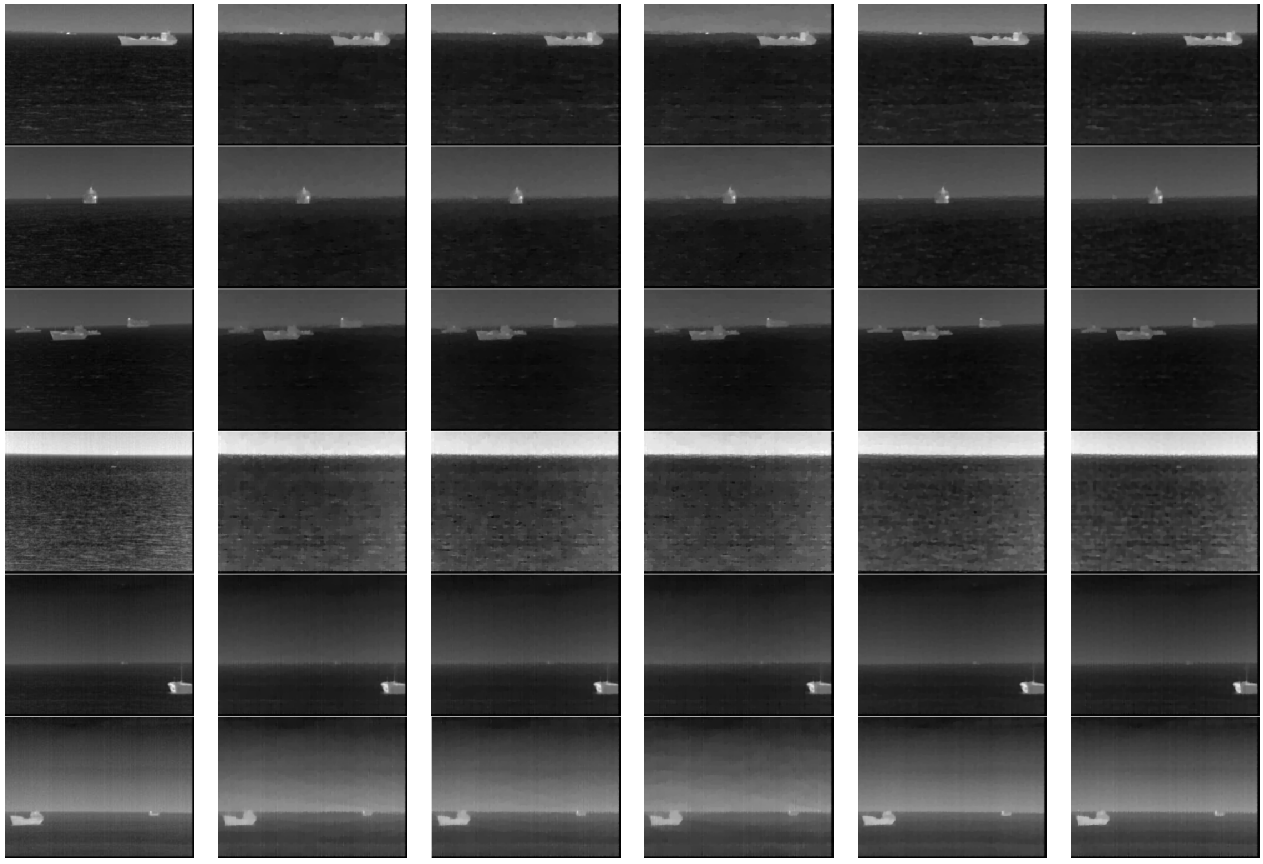

(a)Original (b)P_{Star} (c)$P_{DoubleStar}$ (d)$P_{StarCircle}$ (e)P_{Gauss} (f)P_{Sun}

Fig. 9. Examples of reconstructed images using different sampling patterns for experiment 2.

autocorrelations of the radial patterns preserve their radial manner and they are concentrated at the low frequencies that contain most of the energy.

In both of the experiments, the proposed P_{sun} pattern has fewer samples than the baseline sampling patterns. As an additional experiment, using the

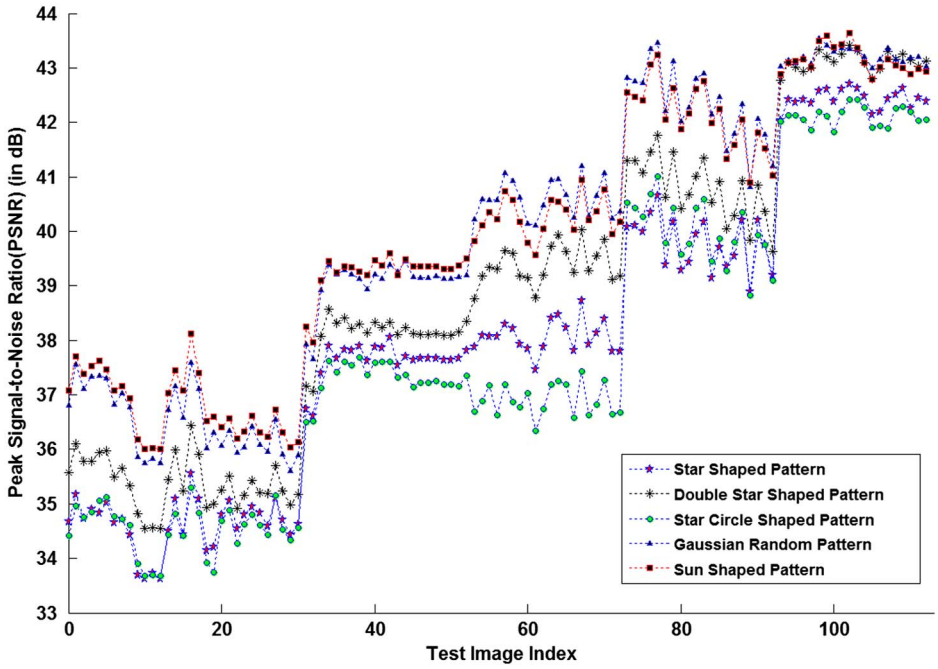

Fig. 10. PSNR ratios of the reconstructed images using different sampling patterns for experiment 2.

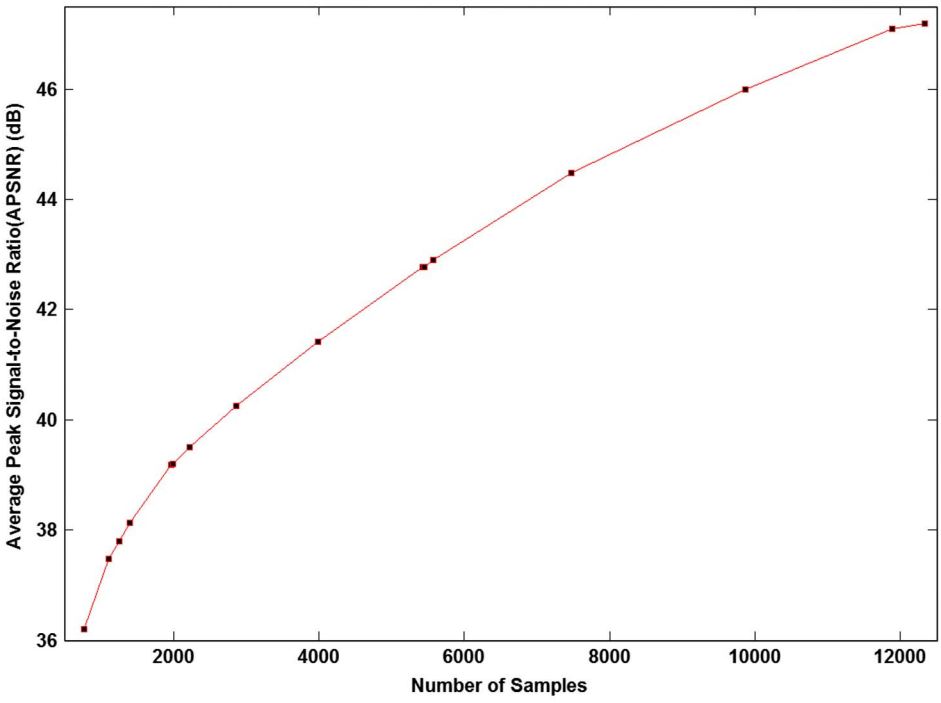

Fig. 11. Relation between the average PSNR values and the sample size of the P_{sun}.

image dataset constructed for the second experiment, the effects of the sample size on the reconstruction performance are observed by using different sample-sized sun-shaped patterns in the reconstruction. The relation between the average PSNR value and sample size is visualized in Fig. 11. From the results presented in this figure, the upward trend in the reconstruction performance can be observed with the increasing number of samples. Because the CS measurement process is progressive, it is quite natural to observe that the reconstruction quality increases with the growing number of samples. However, the CS theory mainly focuses on achieving a better reconstruction performance with a limited number of samples. Therefore, the proposed sampling pattern is suggested to be used rather than the classical sampling methods for better reconstruction performance under the limit of available computational power.

6. Conclusion

In this paper, a novel sampling pattern extraction scheme based on the Fourier characteristics of images collected for sea-surveillance purposes in the IR band is proposed. The proposed sampling pattern is used together with the CS framework for the sparse image recovery problem. Experimental results indicate that the proposed sampling scheme outperforms the baseline sampling methods in the image sparse reconstruction problem. Another advantage of the proposed technique is its efficiency, as it provides higher recovery performance while using fewer samples than classical sampling techniques. The experimental studies also show the generalization capability of the proposed sampling pattern construction technique. By using the statistics of the frequency characteristics of the image database collected for a specific problem, the proposed pattern collecting the important low- and high-frequency components in a clever manner enables higher image reconstruction performance. Therefore, the proposed technique can be used for any sparse image reconstruction problem.

As a future work, we will investigate the application of the proposed sampling technique to old-generation scanning-based pseudoimaging systems in order to convert them into imaging systems by utilizing the scanning pattern in the CS framework.

References

1. R. Baraniuk, "Compressive sensing [lecture notes]," IEEE Signal Process. Mag. **24**(4), 118–121 (2007).
2. E. Candes, J. Romberg, and T. Tao, "Robust uncertainty principles: exact signal reconstruction from highly incomplete frequency information," IEEE Trans. Inf. Theory **52**, 489–509 (2006).
3. D. L. Donoho, "Compressed sensing," IEEE Trans. Inf. Theory **52**, 1289–1306 (2006).
4. M. Duarte, M. Davenport, D. Takhar, J. Laska, T. Sun, K. Kelly, and R. Baraniuk, "Single-pixel imaging via compressive sampling," IEEE Signal Process. Mag. **25**(2), 83–91 (2008).
5. W. L. Chan, M. L. Moravec, R. G. Baraniuk, and D. M. Mittleman, "Terahertz imaging with compressed sensing and phase retrieval," Opt. Lett. **33**, 974–976 (2008).
6. W. L. Chan, K. Charan, D. Takhar, K. F. Kelly, R. Baraniuk, and D. Mittleman, "A single-pixel terahertz imaging system based on compressed sensing," Appl. Phys. Lett. **93**, 121105 (2008).
7. M. Akcakaya and V. Tarokh, "A frame construction and a universal distortion bound for sparse representations," IEEE Trans. Signal Process. **56**, 2443–2450 (2008).
8. E. Candes and T. Tao, "Decoding by linear programming," IEEE Trans. Inf. Theory **51**, 4203–4215 (2005).

9. T. Wan and Z. Qin, "An application of compressive sensing for image fusion," Int. J. Comput. Math. **88**, 3915–3930 (2011).
10. X. Li and S.-Y. Qin, "Efficient fusion for infrared and visible images based on compressive sensing principle," IET Image Process. **5**, 141–147 (2011).
11. J. Ma, "A single-pixel imaging system for remote sensing by two-step iterative curvelet thresholding," IEEE Geosci. Remote Sens. Lett. **6**, 676–680 (2009).
12. J. Ma, "Single-pixel remote sensing," IEEE Geosci. Remote Sens. Lett. **6**, 199–203 (2009).
13. J. Bobin, J.-L. Starck, and R. Ottensamer, "Compressed sensing in astronomy," IEEE J. Sel. Top. Signal Process. **2**, 718–726 (2008).
14. V. Cevher, A. Sankaranarayanan, M. F. Duarte, D. Reddy, and R. G. Baraniuk, "Compressive sensing for background subtraction," in *Proceedings of the European Conference on Computer Vision* (Springer, 2008), pp. 155–168.
15. Y. Kashter, O. Levi, and A. Stern, "Optical compressive change and motion detection," Appl. Opt. **51**, 2491–2496 (2012).
16. H. Li, C. Shen, and Q. Shi, "Real-time visual tracking using compressive sensing," in *Proceedings of the IEEE Conference on Computer Vision and Pattern Recognition* (IEEE, 2011), pp. 1305–1312.
17. D. Reddy, A. Sankaranarayanan, V. Cevher, and R. Chellappa, "Compressed sensing for multi-view tracking and 3-d voxel reconstruction," in *Proceedings of the IEEE International Conference on Image Processing* (IEEE, 2008), pp. 221–224.
18. V. M. Patel, N. M. Nasrabadi, and R. Chellappa, "Sparsity-motivated automatic target recognition," Appl. Opt. **50**, 1425–1433 (2011).
19. J. Duarte-Carvajalino and G. Sapiro, "Learning to sense sparse signals: simultaneous sensing matrix and sparsifying dictionary optimization," IEEE Trans. Image Process. **18**, 1395–1408 (2009).
20. J. Mairal, G. Sapiro, and M. Elad, "Learning multiscale sparse representations for image and video restoration," Multiscale Model. Simul. **7**, 214–241 (2008).
21. S. Ji, Y. Xue, and L. Carin, "Bayesian compressive sensing," IEEE Trans. Signal Process. **56**, 2346–2356 (2008).
22. M. Elad, "Optimized projections for compressed sensing," IEEE Trans. Signal Process. **55**, 5695–5702 (2007).
23. I. Ramirez and G. Sapiro, "Universal regularizers for robust sparse coding and modeling," IEEE Trans. Image Process. **21**, 3850–3864 (2012).
24. D. Wipf, J. Palmer, and B. Rao, "Perspectives on sparse Bayesian learning," in *Proceedings of the Advances in Neural Information Processing Systems* (MIT, 2004), Vol. **16**.
25. E. Candes and J. Romberg, "Sparsity and incoherence in compressive sampling," Inverse Probl. **23**, 969 (2007).
26. M. Wakin, J. Laska, M. Duarte, D. Baron, S. Sarvotham, D. Takhar, K. Kelly, and R. Baraniuk, "An architecture for compressive imaging," in *2006 IEEE International Conference on Image Processing*, October 2006 (IEEE, 2006), pp. 1273–1276.
27. L. I. Rudin, S. Osher, and E. Fatemi, "Nonlinear total variation based noise removal algorithms," Physica D **60**, 259–268, 1992.
28. M. P. Friedlander, "SPGL1," UBC Computer Science, Scientific Computing Laboratory, July 2009, http://www.cs.ubc.ca/~mpf/spgl1.
29. D. L. Donoho, V. Stodden, and Y. Tsaig, "About SparseLab," Stanford University, Version 2.0, March 2007, http://sparselab.stanford.edu.
30. E. Candes and J. Romberg, "ℓ_1-magic: recovery of sparse signals via convex programming," 2005, www.acm.caltech.edu/l1magic/downloads/l1magic.pdf.
31. H. Mohimani, M. Babaie-Zadeh, and C. Jutten, "A fast approach for overcomplete sparse decomposition based on smoothed ℓ_0 norm," IEEE Trans. Signal Process. **57**, 289–301 (2009).
32. Y. Le Montagner, E. Angelini, and J.-C. Olivo-Marin, "Comparison of reconstruction algorithms in compressed sensing applied to biological imaging," in *Proceedings of the IEEE International Symposium on Biomedical Imaging: From Nano to Macro* (IEEE, 2011), pp. 105–108.
33. Z. Wang, *New Sampling and Detection Approaches for Compressed Sensing and Their Application to Ultra Wideband Communications* (Proquest, 2011).
34. Y.-C. Kim, S. S. Narayanan, and K. S. Nayak, "Accelerated three-dimensional upper airway MRI using compressed sensing," Magn. Reson. Med. **61**, 1434–1440 (2009).
35. S. Boyd and L. Vandenberghe, *Convex Optimization* (Cambridge University, 2004).
36. Z. Wang and A. Bovik, "A universal image quality index," IEEE Signal Process. Lett. **9**, 81–84 (2002).